https://doi.org/10.5194/egusphere-2026-2598
Preprint. Discussion started: 20 May 2026

A basin-scale mapping method for crevasse depth using ICESat-2: a case study on Greenland's Sermeq Kujalleq (Jakobshavn Isbræ)

Ruijie Chang[1,5], Xi Lu[2], Ronggang Huang[1], Andrew J. Sole[3], Stephen J. Livingstone[3], Zhen Dong[4], Liming Jiang[1,5], Hansheng Wang[1], Bisheng Yang[4]

[1] State Key Laboratory of Precision Geodesy, Innovation Academy for Precision Measurement Science and Technology, Chinese Academy of Sciences, Wuhan, 430071, China
[2] School of Geography and Sustainable Development, University of St Andrews, St Andrews, KY16 9AL, UK
[3] School of Geography and Planning, University of Sheffield, Sheffield, S10 2TN, UK
[4] State Key Laboratory of Information Engineering in Surveying, Wuhan University, Wuhan, 430072, China
[5] College of Earth and Planetary Science, University of Chinese Academy of Sciences, Beijing, 100049, China

Correspondence: Ronggang Huang (ronggang.huang@apm.ac.cn)

Abstract

Surface crevasses across the Greenland Ice Sheet remain a major source of uncertainty in understanding mass loss processes, including calving, ice flow, and meltwater routing. Most previous studies have primarily focused on the two-dimensional characteristics of surface crevasses on the Greenland Ice Sheet, measurement of crevasse depth, especially from catchment to ice-sheet scale, is limited, thereby limiting our ability to quantify their impact on ice-sheet stability and surface hydrology. The ICESat-2 ATL03 data (0.7 m resolution) provide an unprecedented

https://doi.org/10.5194/egusphere-2026-2598
Preprint. Discussion started: 20 May 2026

opportunity to measure crevasse depths, yet large-scale applications are hindered by challenges such as massive data volume and noises. Here, we develop an automated and efficient ICESat-2 method for crevasse depth estimation that rapidly identifies crevassed regions using a novel roughness index, retrieves signal photons via a similarity-based weighted density approach, and extracts crevasses for depth estimation using a local extrema method. A total of 18,775 crevasse locations were detected from 2,286 beams on Sermeq Kujalleq in 2019. The average crevasse depth is 7.20 ± 0.03 m, with depth maxima occurring at approximately 20 km and 10 km inland in the south and north ice streams, respectively. Crevasses in the northern ice stream are mainly distributed below 600 m a.s.l, whereas those in the southern ice stream predominantly occur below 900 m a.s.l. Compared to IceBridge ATM data, the RMSE of crevasse depths estimated from the ATL03 product is 0.97 m, 5.30 m lower than that from ATL06. In addition, ATL03-derived depths are approximately 28% and 30% deeper than those from ATL06 and ArcticDEM. This study enables metre-scale crevasses to be incorporated into large-scale analyses of ice dynamics and calving, and highlights the potential of ICESat-2 for large-scale crevasse depth estimation, providing valuable insights for global crevasse mapping.

1. Introduction

Greenland Ice Sheet (GrIS) is the second largest ice mass in the world, contributing about 8.9 mm to global sea-level rise from 2003-2019 (Jones et al., 2021; Smith et al., 2020). During the past four decades, its mass loss has accelerated six-fold due to increased surface meltwater runoff and retreat of marine-terminating outlet glaciers (King et al., 2020; Mouginot et al., 2019; Shepherd, 2020). Understanding the underlying processes, such as meltwater routing, crevasse propagation, and calving dynamics, remains critical for predicting future glacier evolution. (Benn et al., 2007; Berg and Bassis, 2022; Zarrinderakht et al., 2022). Surface crevasses form when local tensile or shear stresses in ice exceed its strength (Vaughan, 1993), providing a key

https://doi.org/10.5194/egusphere-2026-2598
Preprint. Discussion started: 20 May 2026

route for delivering surface meltwater into ice bed, and affect ice dynamics by changing the basal water pressure or weakening basal sediment (Chandler and Hubbard, 2023; Fountain et al., 2005; Lai et al., 2020). Additionally, propagation of surface crevasses can result in glacier calving events (Bassis and Ma, 2015; Benn et al., 2007; Berg and Bassis, 2022; Walker and Gardner, 2019). It is therefore necessary to monitor crevasses to understand ice motion and assess glacier vulnerability.

Most previous works have focused on the two-dimensional characteristics of surface crevasses (e.g., length, width, and orientation) and their evolution using optical and synthetic aperture radar imagery (Colgan et al., 2011; Lampkin et al., 2013; Zhao et al., 2022). However, crevasse depth is also a key factor influencing glacier stability, as deeper crevasses facilitate meltwater delivery to the ice bed, potentially enhancing basal sliding and accelerating ice flow (Colgan et al., 2016). Currently, crevasse depths have been detected using ground, airborne or satellite remote sensing technologies in published works, such as ground-penetrating radar (GPR), stereophotogrammetry, and laser altimetry (Huang et al., 2019; Li et al., 2021; Liu et al., 2014; Ryan et al., 2015; Wang et al., 2021; Williams et al., 2014). Although airborne and ground-based remote sensing technologies can detect the vertical structures of crevasses, they are best suited to very small regions (Huang et al., 2019; Williams et al., 2014). Thus, satellite remote sensing technologies (e.g., satellite stereophotogrammetry and satellite altimetry) have been employed to detect crevasse depths across larger regions (Chudley et al., 2021, 2025; Li et al., 2021; Liu et al., 2014; Wang et al., 2021). Satellite stereophotogrammetry produces high-resolution elevation products for glacier surfaces, such as the ArcticDEM, from which crevasse depths can be derived (Chudley et al., 2021, 2025). However, generating DEMs from photogrammetry over steep and complex glacier terrain can introduce errors due to poor image texture and terrain conditions, potentially leading to failures or underestimation in detecting crevasse depths, particularly for narrow or small crevasses (Barrand et al., 2009). Satellite altimetry can directly measure surface elevations. The Ice, Cloud, and land Elevation Satellite (ICESat) carries the Geoscience Laser Altimeter System (GLAS) (Abshire et

https://doi.org/10.5194/egusphere-2026-2598
Preprint. Discussion started: 20 May 2026

al., 2005), has been successfully applied to detect depths of large crevasses over Antarctic ice shelves (Fricker et al., 2005; Liu et al., 2014), but its capability in detecting smaller crevasses is limited by its low resolution, such as in Greenland.

The Ice, Cloud and land Elevation Satellite-2 (ICESat-2), launched in 2018, carries the multi-beam micro-pulse photon-counting laser altimeter (ATLAS), with a footprint size and along-track sampling distance of 11 m and 0.7 m, respectively (Markus et al., 2017; Neumann et al., 2019). Similar to studies monitoring the depths of large crevasses using ICESat, researchers have also made significant progress in large crevasses and rifts (with widths exceeding 100 m) detection using the ICESat-2 ATL06 product over the Amery Ice Shelf, Antarctica (Li et al., 2021; Wang et al., 2021). However, the ~20 m spatial resolution of the ICESat-2 ATL06 product will struggle to detect narrower crevasses, which are widely distributed over the GrIS (Chang et al., 2023; Herzfeld et al., 2021; Smith et al., 2019). The ICESat-2 ATL03 product, with a higher resolution of 0.7 m, provides an opportunity to address this problem. Recently, Herzfeld et al. (2021) and Chang et al. (2023) have demonstrated successes in detecting narrow crevasses on the GrIS using a few ICESat-2 ATL03 granules. However, detecting crevasse depths from the ICESat-2 ATL03 product on a large scale, such as a basin scale, has not yet been carried out due to the difficulty and time-consuming process of retrieving glacier surface photons from the large volume of noisy raw data. Quickly and efficiently extracting crevasses and estimating their depths from the ATL03 product therefore remains a non-trivial challenge.

This study proposes an automated and efficient method for surface crevasse extraction and depth estimation based on ICESat-2 ATL03 product in a basin scale, and maps the crevasse depths on Sermeq Kujalleq in 2019. Firstly, we detect crevassed regions by designing a novel roughness index, dramatically reducing the data volume for large-scale glacier-height extraction and crevasse depth mapping. Secondly, we separate glacier surface signal photons from noise photons for each crevassed region based on the similarity weighted density of photons. Thirdly, a local extrema method is employed to extract crevasses and estimate their depths. Finally, we use the proposed

https://doi.org/10.5194/egusphere-2026-2598
Preprint. Discussion started: 20 May 2026

method to map the distributions of crevasse depths on Sermeq Kujalleq in 2019, and analyze their spatial characteristics. To the best of our knowledge, this is the first-time that crevasse depths have been mapped at a basin scale on the GrIS using the ICESat-2 ATL03 product. It provides a new dataset of crevasse depths and a novel solution of crevasse depth mapping to facilitate further investigation of links between crevasses, ice dynamics and calving.

2. Study area and data

2.1 Study area

Sermeq Kujalleq (Jakobshavn Isbræ) (SKJI), located in western Greenland (Fig. 1a), is the largest and fastest outlet glacier of the GrIS and drains about 6.5% of the ice sheet (Joughin et al., 2014; Rignot and Kanagaratnam, 2006). This outlet glacier is characterized by two ice streams: the south ice stream exhibits heavy surface crevassing over a length of 80-100 km, with the shorter north ice stream joining ~12 km upstream from the terminus (Mayer and Herzfeld, 2000). The terminus of SKJI remained relatively stable during the 1990s, but its ice tongue gradually thinned and retreated starting in 1997, ultimately disintegrating completely in 2003 (Podlech and Weidick, 2004; Sohn et al., 1998). After the disintegration of the ice tongue, SKJI continued to accelerate and thin (Joughin et al., 2012). However, influenced by the intrusion of colder ocean waters, SKJI exhibited notable slowdown and thickening during 2016-2019, accompanied by a reduction in crevasse volume (Chudley et al., 2025; Picton et al., 2025). This trend reversed thereafter, SKJI accelerated significantly, with the maximum velocity in summer increasing by 79% (Picton et al., 2025). This rapid ice motion resulted in dense crevassing, particularly near the shear margins and terminus. SKJI's surface crevasses have received less attention compared to its mass balance, the distribution of surface meltwater and its ice motion (Picton et al., 2025; Shepherd, 2020; Zhang et al., 2023).

https://doi.org/10.5194/egusphere-2026-2598
Preprint. Discussion started: 20 May 2026

2.2 ICESat-2 data product

ICESat-2 generates six laser beams arranged in three pairs. Each pair consists of a strong beam and a weak beam (Markus et al., 2017; Neumann et al., 2019). ICESat-2 provides standard products at different levels based on different science purposes, which are available at the National Snow and Ice Data Center (NSIDC, https://nsidc.org/data/icesat-2). The Level 2 data product (ATL03) provides geolocated photons with latitudes, longitudes, and ellipsoidal heights. After the processing of the signal finding algorithm, each photon is assigned a confidence level (*signal_conf_ph*) ranging from 0 to 4. In addition, the ATL03 product also provides a photon weight parameter (*weight_ph*), which can be used to represent photon density. These two parameters of photon weight and confidence level can be used as references for extracting signal photons. However, in crevassed regions, many noise photons are classified as signal with confidence levels greater than 2, and the weights of noise photons are sometimes also assigned a high value and are close to those of signal photons (Fig. 1c and d). Therefore, using only photon weights and confidence levels is insufficient for accurately extracting signal photons, it is necessary to develop an alternative method. In this study, we collected 381 ATL03 granules from 104 tracks over SKJI in 2019, including all strong and weak beams (2,286 beams in total). The spatial distribution of the granules is shown in Fig. 1b. In total, the dataset contains approximately 1.6 billion photons, covering a length of approximately 2.9×10^5km, which poses a significant challenge for data processing. Therefore, efficiently isolating crevassed regions is crucial for improving the efficiency of large-scale crevasse mapping.

https://doi.org/10.5194/egusphere-2026-2598
Preprint. Discussion started: 20 May 2026

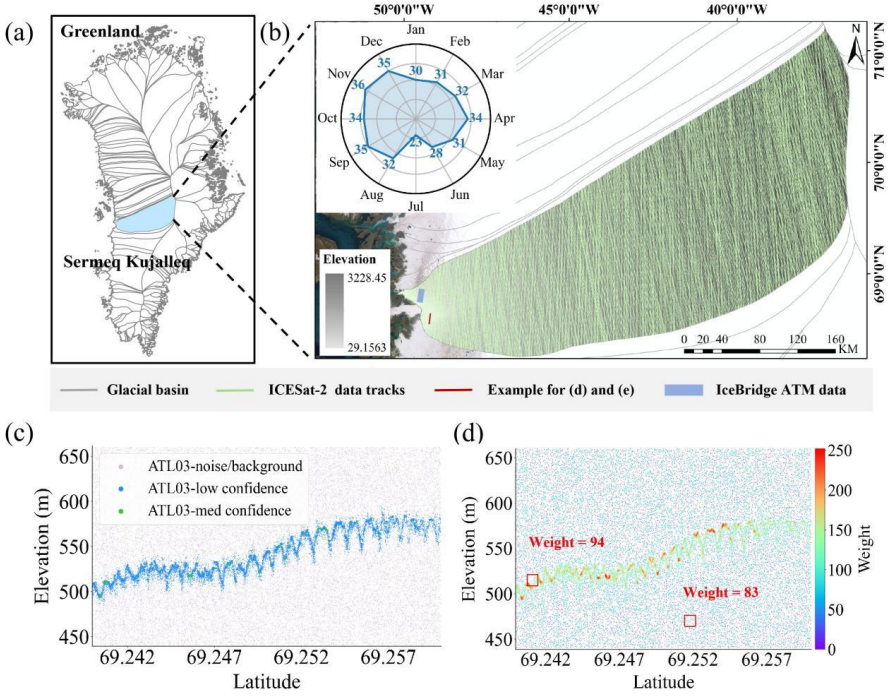

Figure 1. Study area and datasets. (a) SKJI location within the GrIS. (b) The spatial and temporal distribution of the datasets. Numbers in the inset represent the number of granules in each month. (c) and (d) Illustration of confidence photons and photon weights.

3. Methodology

In order to rapidly and efficiently map crevasse depth distribution from the ICESat-2 ATL03 product at SKJI, we developed an automated method for crevasse extraction and depth estimation (Fig. 2). Firstly, we retrieved photons from ATL03 granules acquired in 2019 within the boundary of SKJI, as defined by (Mouginot et al., 2019). The retrieved photons were then preprocessed and filtered based on the confidence levels to remove distinct noises, retaining photons with confidence levels greater than 1 for subsequent processing steps: 1) crevassed region detection; 2) glacier-height retrieval and surface reconstruction; and 3) crevasse extraction and depth estimation.

https://doi.org/10.5194/egusphere-2026-2598
Preprint. Discussion started: 20 May 2026

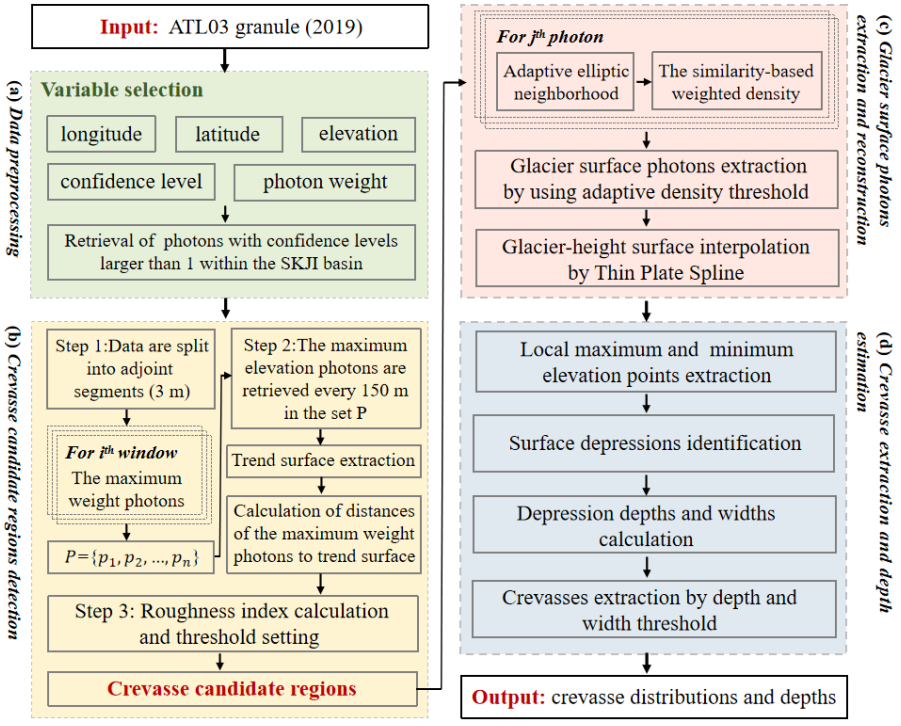

Figure 2. Flowchart of the proposed method.

3.1 Crevassed region detection using a novel roughness index

To improve the efficiency of removing photon noises and detecting crevasses, we first identified regions likely to contain crevasses, thereby avoiding time-consuming data processing of the ATL03 product over the entire basin. Crevasses are characterized as depressions with significant elevation differences, while most other glacier surfaces are relatively flat at a defined scale. Therefore, we detected crevassed regions using a roughness index, which was defined as a statistic of the residual distance from each signal photon in a local neighbor to the corresponding glacier trend surface. However, contamination of signal photons by noise photons in the ATL03 product affected the calculation of the roughness index in local regions. To address this problem, we rapidly retrieved possible signal photons based on photon weight (*weight_ph*) in the ATL03 product, then generated a trend surface to estimate the roughness index approximately.

https://doi.org/10.5194/egusphere-2026-2598
Preprint. Discussion started: 20 May 2026

First, we detected possible signal photons from the ATL03 products, according to the assumption that a photon with a larger weight is more likely to be a signal. Photons with a confidence level >1 in a track of the ATL03 product were split into segments, with the segment size set to a small length (e.g., 3.0 m). The photon with the maximum weight in each segment was extracted as a possible signal photon (Fig. 3a and b), and the extracted possible signal photons in all segments comprised the set P. There may still be noise photons in set P, especially for tracks with low quality, so we removed obvious outliers by the smoothness of photon elevations between adjacent segments. When a photon was significantly higher or lower than neighboring possible signal photons, it was removed from the set P.

Second, we retrieved the photon with the maximum elevation within a neighboring range from the set P, and used these retrieved photons to construct the broad-scale glacier surface. In this study, the neighboring range should exceed the crevasse width in SKJI and is set as 150 m. For each 150 m range along the track in the set P, the photon with the maximum elevation was extracted as a key trend surface photon (Fig. 3a and b) and designated as set *E*. The glacier surface was then interpolated by linking photons in the set *E* sequentially.

Third, a roughness index was estimated between each two neighboring trend surface photons in set E to detect crevassed regions. Possible signal photons were retrieved between each two neighboring trend surface photons from the set P, and the residual distances from these possible signal photons to the glacier trend surface were calculated, forming the set $D = \{d_1, d_2, \dots, d_n\}$. The roughness index, Rq, was then estimated according to Eq.(1).

$$R_q = \sqrt{\frac{\sum_{i=1}^{n} d_i^2}{n}} \quad (1)$$

where d_i is the distance from a possible signal photon to the glacier trend surface; and n is the number of possible signal photons between each two surface photons.

Following testing (e.g., Fig. 3a and b), we used a roughness threshold t_q of 1 to extract crevassed regions at SKJI (Table 1). When the roughness index between two neighboring glacier trend surface photons exceeded t_q, the range between these two

https://doi.org/10.5194/egusphere-2026-2598
Preprint. Discussion started: 20 May 2026

neighboring trend surface photons was classified as a crevassed region, and the corresponding photons within this range were retained for the following steps for crevasse detection and depth estimation. In this way, crevassed regions were detected across the entire basin. To ensure that no crevassed regions were missed, we buffered an additional 300 m of data around the detected crevassed regions.

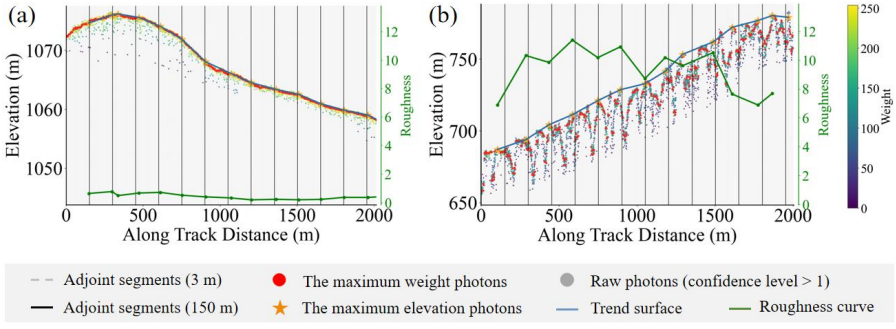

Figure 3. Illustration of roughness index calculation for a smooth region (a) and a crevassed region (b).

3.2 Glacier surface photon extraction

After detection of crevassed regions, we extracted glacier surface photons by separating signal photons from noises. In our previous work, Chang et al. (2023) proposed a robust density estimation method for glacier-height retrieval from the ATL03 product using two strategies: (1) selection of the optimal elliptical neighborhood for each photon; and (2) development of a hybrid weighted photon density considering spatial context. To improve computational efficiency for large-scale processing, we adopted a simplified version of this approach. Specifically, instead of selecting the optimal elliptical neighborhood for each photon using multi-scale RANSAC, we fixed the neighborhood size (a=10 m, b=0.7 m; Table 1) based on sensitivity experiments reported in Chang et al. (2023). Second, the hybrid weighted photon density considered the smoothness of the glacier surface and the spatial similarity of neighboring photons. However, the smoothness-based weighted density was affected by complex morphology with varying scales in crevassed regions, causing a decrease in

https://doi.org/10.5194/egusphere-2026-2598
Preprint. Discussion started: 20 May 2026

243 performance. Therefore, we only use the similarity-based weighted density for glacier
244 surface photon extraction in this study, as defined in Eqs. (2) and (3).

245 $$w_{sm}^{i} = \frac{1}{\sigma_{sm}\sqrt{2\pi}} e^{-\frac{pd_i^2}{2\sigma_{sm}^2}} \quad (2)$$

246 where w_{sm}^{i} is the smoothness-based weight of photon i, σ_{sm} is the standard
247 deviation, pd_i is the distance of photon i to the fitting line.

248 $$f_{sm}(p) = \sum_{i \in N_p} w_{sm}^{i} \quad (3)$$

249 where N_p represents the neighboring photons of photon p, and $f_{sm}(p)$ is the
250 smoothness-based weighted density of photon p.

251 After calculation of the similarity-based weighted density for each photon, the
252 photons within each crevassed region were split into segments, and glacier surface
253 photons were extracted by an adaptive threshold for each segment. Details about the
254 similarity-based weighted density and the auto-adaptive threshold for signal photon
255 extraction can be found in Chang et al. (2023). For each crevasse region, Thin Plate
256 Spline interpolation (TPS) (Hingee et al., 2019) was utilized to reconstruct the glacier
257 surface based on extracted signal photons into one-dimensional elevation profile. This
258 approach reduced the influence of location errors of photons and filled void regions of
259 missing photons, especially for crevasse sidewalls. A case is shown in Fig. 4.

260 ### 3.3 Crevasse extraction and depth estimation

261 Crevasse extraction includes two steps: extracting surface depressions and
262 identifying crevasses.

263 ***Step 1: Extraction of surface depressions.*** We used a local extrema method to
264 detect surface depressions within the reconstructed one-dimensional elevation profile
265 of each crevassed region. First, local extrema points, including minimum and maximum
266 elevation points, were extracted from the TPS interpolated elevation profile (Fig. 4).
267 For each minimum elevation point, we found the nearest maximum elevation points on
268 the left and right, respectively. If the range between the minimum elevation point and

https://doi.org/10.5194/egusphere-2026-2598
Preprint. Discussion started: 20 May 2026

the neighboring maximum elevation points did not contain any other minimum elevation points, the range between one minimum elevation point and the two neighboring maximum elevation points was taken as a surface depression.

Step 2: Identification of crevasses. In addition to crevasses, surface depressions can also include supraglacial river channels, topographic undulations or others. Compared to other surface depressions, crevasses are relatively deep compared to their width. Therefore, the depression depth (D_c) and depression width (W_c) were calculated. The depression depth is defined as the elevation difference between the maximum and minimum points of a depression feature, while the distance between the two maximum elevation points is taken as its width, as shown in Fig. 4. The corresponding rules were established to identify crevasses, as defined in Eq. (4).

$$\begin{cases} W_c < W_0 \\ D_c > D_0 \end{cases} \tag{4}$$

where the crevasse width should not exceed the maximum width threshold W_0, and the crevasse depth should not be shallower than the minimum depth threshold D_0 (Table 1).

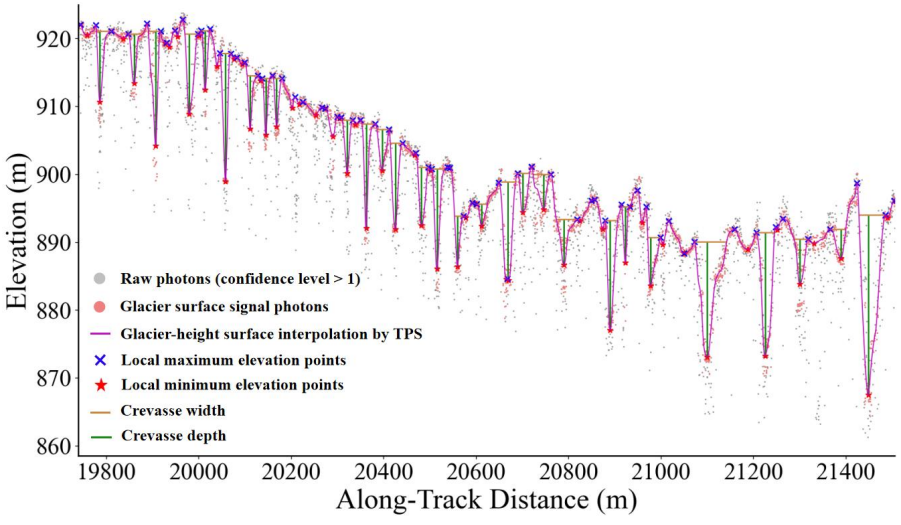

Figure 4. Illustration of glacier surface photon extraction, ice surface reconstruction and crevasse metric extraction.

https://doi.org/10.5194/egusphere-2026-2598
Preprint. Discussion started: 20 May 2026

3.4 Evaluation Metrics

To evaluate the performance of crevasse extraction and depth estimation, we employed two schemes. First, we manually analyzed the ATL03 photon profiles to validate each key step, including crevassed region detection, glacier surface photon extraction, and crevasse extraction, and then calculated Precision (P), Recall (R) and F_1 scores, as shown in Eqs. (5)-(7).

$$P = \frac{TP}{TP+FP} \tag{5}$$

$$R = \frac{TP}{TP+FN} \tag{6}$$

$$F_1 = 2 \times \frac{P \times R}{P+R} \tag{7}$$

where TP, FP, and FN denote true positives, false positives, and false negatives, respectively, representing correctly identified, incorrectly identified, and missed samples.

Secondly, the estimated crevasse depth was evaluated against IceBridge ATM data acquired on the same day (May 15th, 2019), where Root Mean Square Error (RMSE) and Coefficient of Determination (R^2) were calculated, as shown in Eqs. (8) and (9).

$$RMSE = \frac{\sqrt{\sum_{i=1}^{n}(y_i - x_i)^2}}{n} \tag{8}$$

$$R^2 = 1 - \frac{\sum_{i=1}^{n}(y_i - x_i)^2}{\sum_{i=1}^{n}(y_i - \bar{y})^2} \tag{9}$$

where x_i is the crevasse depth calculated by the ICESat-2 product, y_i is the crevasse depth calculated by the IceBridge ATM data, and $\bar{y}$ is the average of the crevasse depth calculated by the IceBridge ATM data.

Table 1. Parameter settings

Parameter	Value	Description
t_q	1	The threshold for the roughness index is used to detect crevassed regions.
a	10 m	The semi-major axis of the elliptical neighborhood.
b	0.7 m	The semi-minor axis of the elliptical neighborhood.

https://doi.org/10.5194/egusphere-2026-2598
Preprint. Discussion started: 20 May 2026

σ_{sm}	0.5	The standard deviation in the calculation of the smoothness-based weight.
W_0	150 m	The width threshold applied in crevasse extraction.
D_0	3 m	The depth threshold applied in crevasse extraction.

4. Results

We calculated the spatial distribution of crevasses and their depths across SKJI in 2019 using the ICESat-2 photon tracks and parameter settings shown in Table 1. As follows, we present the accuracy assessment of each key step in the proposed method and an analysis of the results.

4.1 Algorithm performance evaluation

We selected ICESat-2 photon tracks acquired between January 2019 and March 2019 to evaluate the performance of crevasse region detection, glacier surface photon retrieval and crevasse extraction.

4.1.1 Evaluation of crevassed region detection

Results of crevassed region detection from ICESat-2 photon tracks for SKJI in 2019 are shown at Fig. 5a and b, where most of the basin does not contain crevasses (90.75%), and crevassed regions are mainly distributed at the glacier front. It shows that the processing of crevassed region detection significantly reduces data volume, and enhances computational efficiency, which is key for extracting crevasses at the basin-scale. According to the quantitative evaluation results in Table 2, the proposed method achieves high accuracies, with F1-scores of 0.925 and 0.960 for weak and strong beams, respectively. More importantly, the recall of the proposed method is close to 1, indicating that nearly all the crevassed regions are correctly identified, as shown for two cases in Fig. 5f and g. However, the precision is considerably lower than the recall. The values of precision only achieve 0.896 and 0.922 for the weak and strong beams,

https://doi.org/10.5194/egusphere-2026-2598
Preprint. Discussion started: 20 May 2026

which are 0.059 and 0.078 lower than the corresponding recalls. This is mainly because: 1) when calculating the trend surface, if the window is too large, some regions with steep slopes are treated as crevassed regions, as shown in Fig. 5h; and 2) there are other glacier features mistakenly detected as crevasse regions, such as supraglacial lakes, supraglacial rivers and ice cliffs, which also exhibit significant elevation differences.

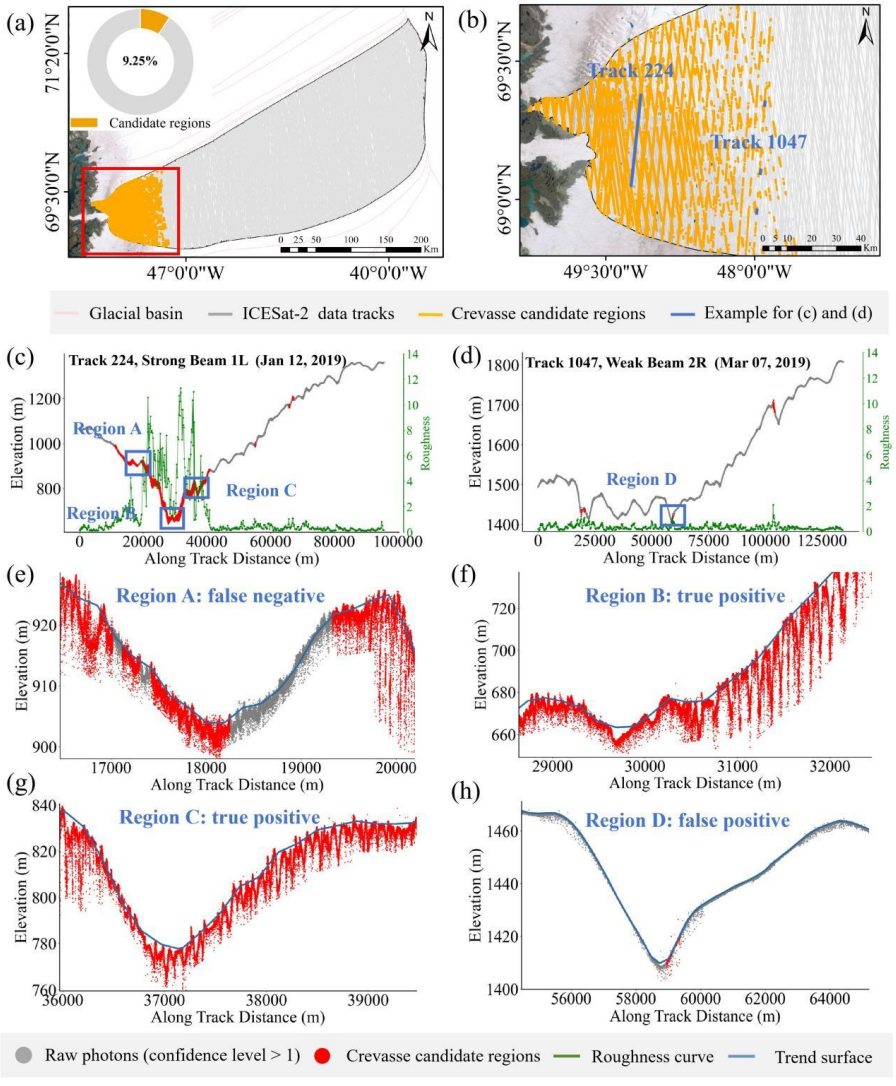

Figure 5. Evaluation results of crevassed region detection. (a) and (b) Extracted crevassed regions, where (b) is the red box in (a). (c) and (d) Results of roughness calculations and

https://doi.org/10.5194/egusphere-2026-2598
Preprint. Discussion started: 20 May 2026

crevassed region detection for two beams. (e)-(h) Cases of crevassed region detection, where (e) shows a false negative, (f) and (g) show true positive, (h) shows a false positive.

4.1.2 Glacier surface photon retrieval evaluation

The proposed method can efficiently extract signal photons for complex ice surfaces, regardless of strong or weak beams, as shown of two cases in Fig. 6a and b. More specifically, the proposed method can efficiently remove noises (Fig. 6f), and can preserve the geometric characteristics of surface crevasses well, such as their bottoms and walls (Fig. 6c-e). Table 2 shows the quantitative evaluation of the results. The proposed method achieved average F1-scores of 0.929 and 0.900 for strong and weak beams, respectively. However, the recalls are 0.105 and 0.108 lower than the precision for strong and weak beams. The main reasons include: 1) an overly large adaptively estimated density threshold, leading to some signal photons being missed; and 2) directions of the elliptical neighborhoods for some signals have slight biases when signal photons are too sparse.

4.1.3 Crevasse extraction evaluation

Figure 7a-f and Table 2 show the evaluation results of crevasse extraction. The results show that the proposed method can correctly extract most of the crevasses, with F1-scores reaching 0.863 and 0.894 for weak and strong beams, respectively. Figure 7c and d show examples of False Positives and False Negatives. False positives may be caused by small topographical folds on the glacier surface or errors in glacier surface reconstruction using the Thin Plate Spline. False negatives are sometimes associated with a smooth and flat bottom of the crevasse (Fig. 7d), making it fail to extract a local minimum point.

https://doi.org/10.5194/egusphere-2026-2598
Preprint. Discussion started: 20 May 2026

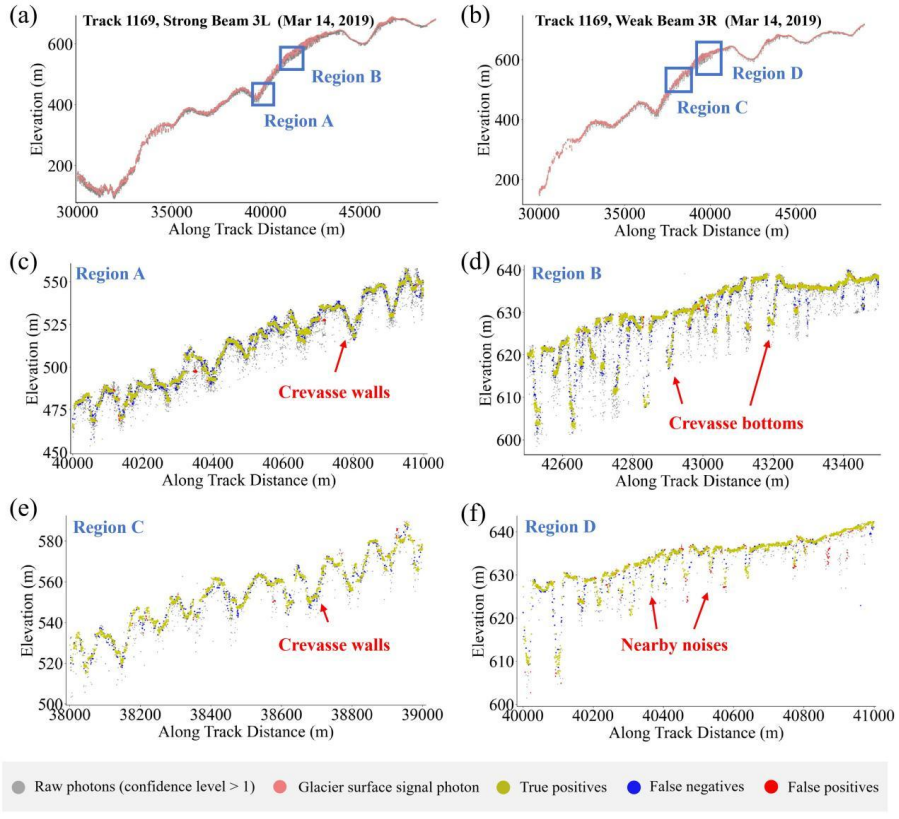

Figure 6. Evaluation results of glacier surface photon retrieval. (a) and (b) Results of glacier surface photon extraction in crevassed regions. (c)-(f) Small scale examples of glacier surface photon extraction, where (c)-(e) show the geometric characteristics of surface crevasses retained by the method, and (f) shows that the method performs well in removing nearby noises.

https://doi.org/10.5194/egusphere-2026-2598
Preprint. Discussion started: 20 May 2026

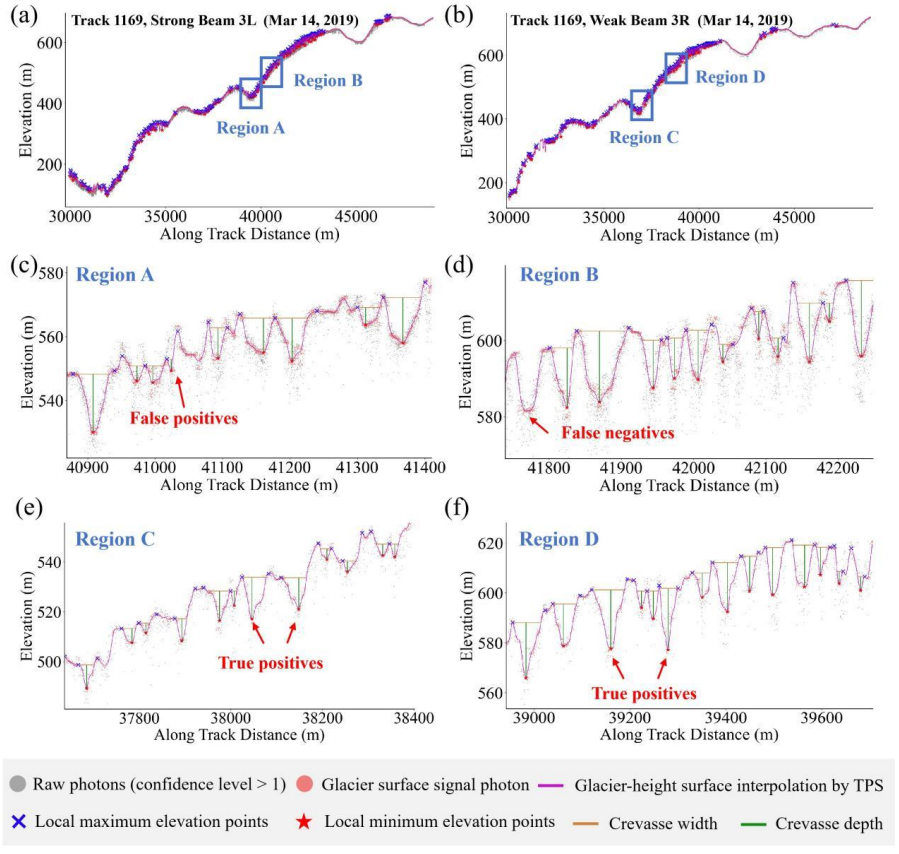

Figure 7. Evaluation results of crevasse extraction. (a) and (b) are the crevasses extracted from the crevassed regions. (c)-(f) are example cases of false positives, false negatives and true positives.

Table 2. Quantitative performance evaluation for key steps of the proposed method

	Weak beam			Strong beam		
	P	R	F_1	P	R	F_1
Crevassed region detection	0.896	0.955	0.925	0.922	1.000	0.960
Glacier photon retrieval	0.958	0.850	0.900	0.984	0.879	0.929
Crevasse extraction	0.846	0.880	0.863	0.877	0.912	0.894

https://doi.org/10.5194/egusphere-2026-2598
Preprint. Discussion started: 20 May 2026

4.1.4 Evaluation of crevasse depth and location

IceBridge ATM data were used to validate crevasse depths estimated from the ICESat-2 ATL03 product, with both acquired on May 15, 2019. A visual comparison (Fig. 8b) suggests the elevation profile from ICESat-2 shows good agreement with the ATM data. We manually interpreted all crevasses within the crevassed region in the ATM data as the reference and compared them to corresponding crevasses derived from the ATL03 product, as shown in Fig. 8b and c. The R^2 and RMSE reach 0.94 and 0.97 m. The minimum and maximum difference between crevasse depths detected by ATL03 and ATM data are 0.06 m and 2.75 m. The results show that the crevasse depths derived from the ICESat-2 AT03 product are reliable.

In addition to depth validation, we also assessed the accuracy of crevasse location using Planet imagery. We performed a visual comparison with optical high-resolution (3 m) Planet images collected over SKJI on May 12, 2019. The corresponding crevasse locations were derived from ICESat-2 photons of the track gt3l of RGT 666, which was captured on May 11, 2019. To reduce the influence of ice motion, we applied a shift correction using the ice velocity product (Solgaard and Kusk, 2022), with a reported velocity of 2.72 m/day. A visual display of the crevasse locations superimposed on the Planet image is shown in Fig. 9a. The detected crevasse locations all coincide with crevasses in the image (bright/dark linear features on the image). To quantitatively assess the accuracy of the extracted crevasse locations, we manually delineated 14 crevasse centerlines from the Planet image, corresponding to 14 detected crevasse locations. The residual distances between each detected crevasse location and its corresponding crevasse centerline in Planet imagery are then calculated (Fig. 9c). Statistically, all residual distances are less than 7 m, with an average residual distance of 2.66 m, which is within the positional uncertainty of the Planet imagery (Semple et al., 2023). Of course, the evaluation accuracy may be influenced by several factors, and it can only be a reference to demonstrate the effectiveness of the detected crevasse locations from ICESat-2 photon tracks. For example, crevasses centerlines delineated

https://doi.org/10.5194/egusphere-2026-2598
Preprint. Discussion started: 20 May 2026

from Planet image may not represent the deepest location of the crevasse, which is likely to induce some error.

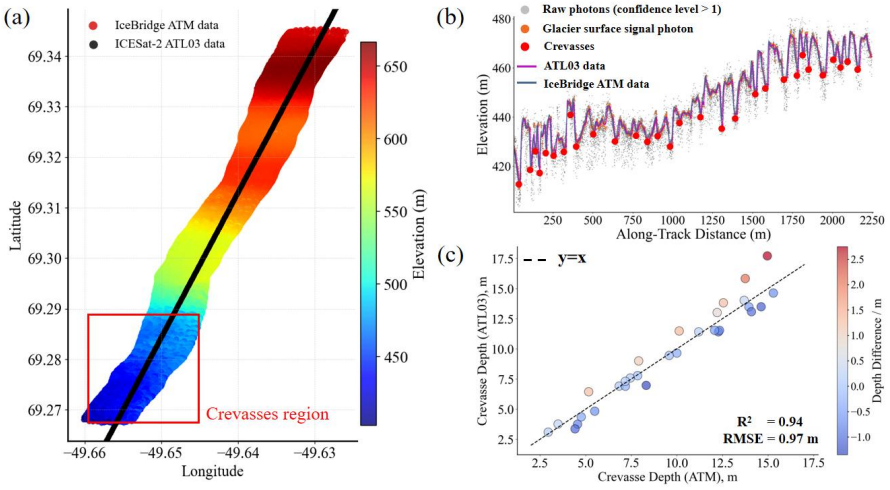

Figure 8. Comparison of crevasse depths derived from ICESat-2 products and IceBridge ATM data. (a) Photon track of ICESat-2 and Icebridge ATM point clouds. (b) Elevation profiles and crevasse detection results from ATL03 and ATM. (c) RMSE and R^2 for crevasse depth results derived from ATL03 product and Icebridge ATM point clouds.

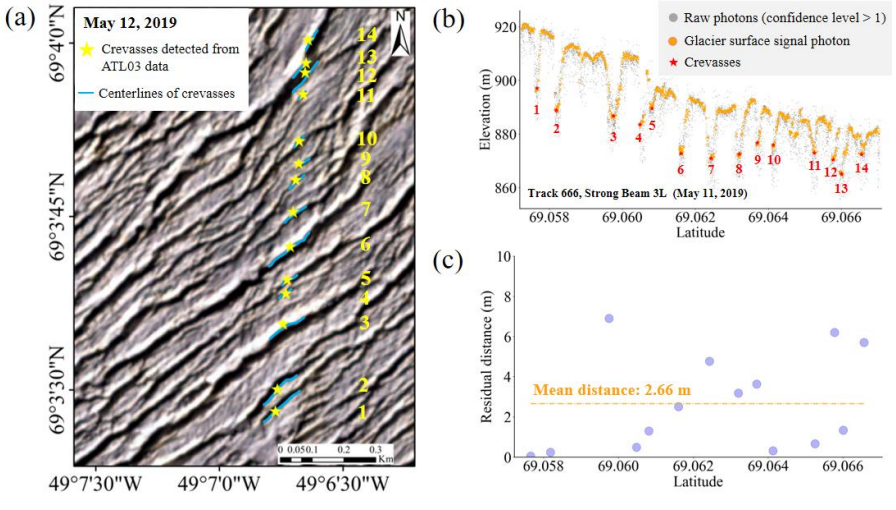

Figure 9. Accuracy assessment of extracted crevasse locations based on a 3 m resolution optical Planet image. (a) Crevasses detected from ATL03 data are superimposed on the Planet image.

https://doi.org/10.5194/egusphere-2026-2598
Preprint. Discussion started: 20 May 2026

(b) Extracted crevasse locations. (c) Residual distances between crevasse locations extracted from ICESat-2 and manually delineated crevasse centerlines from Planet image.

4.2 Distribution and depth characteristics of crevasses on SKJI

In the SKJI basin, we identified 18,775 surface crevasse locations (Fig. 10a) from 104 ICESat-2 ATL03 tracks collected in 2019. Our approach can resolve metre-scale crevasses, down to 7 m, as shown in Fig. 10b. To minimize the effects of sparse ICESat-2 tracks, we analyzed crevasse density by splitting the glacier basin into 5 km by 5 km grid cells, and counting the number of crevasse locations for each grid as crevasse density. Results show that heavily crevassed grid cells are mainly distributed from the glacier terminus to ~10 km inland along the north ice stream, whereas they extend up to ~25 km inland along the south ice stream, suggesting stronger extensional stresses or wider shear margins in the latter. By retrieving elevations of each crevasse location from the ArcticDEM mosaic (Porter et al., 2023) (Fig. 10a), we find that crevasses in the northern ice stream are mainly distributed below 600 m a.s.l, whereas those in the southern ice stream predominantly occur below 900 m a.s.l. In addition, we find that up to 500 m a.s.l, the number of crevasses gradually increases. From 600 m a.s.l to 700 m a.s.l, the number of crevasses slightly decreases due to the decrease in the number of crevasses on the north ice stream. Higher than 700 m a.s.l, the number of crevasses increased again, reaching a second peak around 800 m a.s.l. This bimodal elevation distribution likely reflects distinct strain regimes near the terminus and further inland. Because ICESat-2 ground tracks are spatially sparse, our inventory likely represents a possible estimate of the true crevasses. Nevertheless, the spatial patterns reveal that surface damage is widespread and persistent, particularly on the south ice stream, which might have implications for ice flow acceleration and future terminus retreat (Mayer and Herzfeld, 2000).

The crevasse depth distributions across SKJI in 2019 are presented in Fig. 10a,

https://doi.org/10.5194/egusphere-2026-2598
Preprint. Discussion started: 20 May 2026

with a statistical analysis in Fig. 11. In 2019, the average crevasse depth is 7.20 ± 0.03 m, and the 90th percentile depth is 13.80 m. To compare the difference in crevasse depths between the north and south ice streams, we calculated the average crevasse depth and standard error for each ice stream. Results show that the south ice stream exhibits deeper crevasses, with mean depths approximately 0.2 m greater than the glacier-wide average. This may be due to the faster flow velocity of the south ice stream (Joughin et al., 2012), resulting in increased stress causing propagation of crevasses in the vertical direction. We split the glacier basin into parallel strips with a width of 5 km along the ice flow direction from the terminus and assign detected crevasse locations into corresponding strips. The average crevasse depth for each strip of the two ice streams is calculated and analyzed, as shown in Fig. 11b. In the north ice stream, within 10 km inland from the margin, the average crevasse depth ranges from 7 m to 8 m. Between 10 and 25 km inland from the margin, the crevasse depth gradually decreases, and beyond 25 km, it stabilizes at a relatively constant value (4 m). For the south ice stream, crevasse depth initially gradually increases, reaching a peak (8 m) at around 20 km. Between 20 and 40 km inland from the margin, the crevasse depth gradually decreases, and beyond 40 km, it stabilizes at a relatively constant value (4 m). In both ice streams, standard errors are relatively small near the terminus and gradually increase inland. This pattern likely reflects the greater heterogeneity of crevasse depths farther inland, where crevasses are more sparsely distributed.

https://doi.org/10.5194/egusphere-2026-2598
Preprint. Discussion started: 20 May 2026

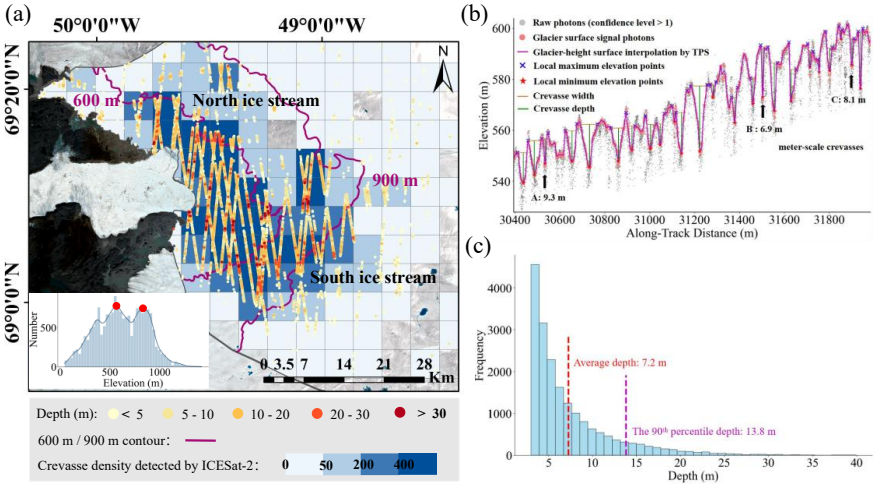

Figure 10. Crevasse extraction results and statistical analysis. (a) Distribution of crevasse locations and depths, with an inset showing crevasse distribution based on elevation statistics. (b) Illustration of meter-scale crevasses. (c) Annual histograms of crevasse depth.

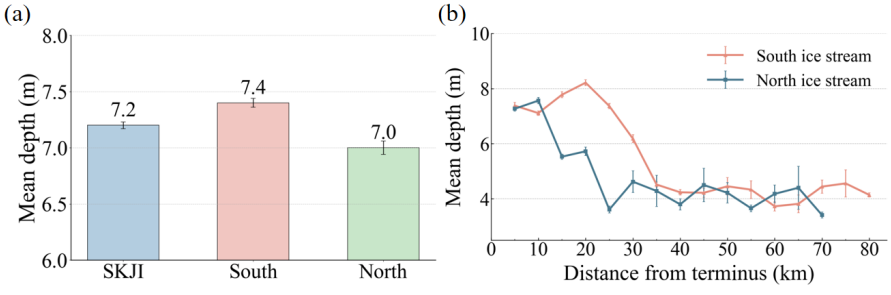

Figure 11. Statistical analysis of crevasse depths in SKJI. (a) Crevasse depths in SKJI, the south ice stream, and the north ice stream. (b) Spatial distribution of crevasse depths along different ice streams in SKJI.

https://doi.org/10.5194/egusphere-2026-2598
Preprint. Discussion started: 20 May 2026

5. Discussion

5.1 Comparison with crevasse locations and depths derived from ATL06 Product

The ATL06 product, aggregated from ATL03 photon data, is generated for land ice but has a relatively low spatial resolution (i.e., 20 m) (Smith et al., 2019). As such, narrow crevasses cannot be detected by the ATL06 product, and crevasse depths are more likely to be underestimated relative to the ATL03 product (Fig. 12c Region A and B). To further validate the necessity for crevasse depth derived from the ATL03 product, we compared crevasse detection and depth estimation results for both ATL03 and ATL06 products over SKJI in 2019.

Figure 12a shows the crevasse depth differences derived simultaneously from the ATL03 and ATL06 products. For the same crevasses, the depths detected by the ATL03 product are deeper by 2.1 m on average than those detected by the ATL06 product. More importantly, many narrow crevasses identified by the ATL03 product are missed by the ATL06 product (Fig. 10 and Fig. 12a). In 2019, 51.8% of the crevasse locations extracted by ATL03 were missed by ATL06, and the missed crevasses had an average depth of 6.4 m and a maximum depth of 38.8 m. We also evaluated the accuracy of crevasse depths derived from the ATL06 product with the IceBridge ATM (Fig. 12b). Crevasse depths derived from the ATL06 product are significantly underestimated. The RMSE is 6.27 m, which is significantly worse than that of the ATL03 product. Compared to crevasse depths derived from the ATL06 product, the accuracy of crevasse depths derived from the ATL03 product improves the RMSE by 5.30 m.

https://doi.org/10.5194/egusphere-2026-2598
Preprint. Discussion started: 20 May 2026

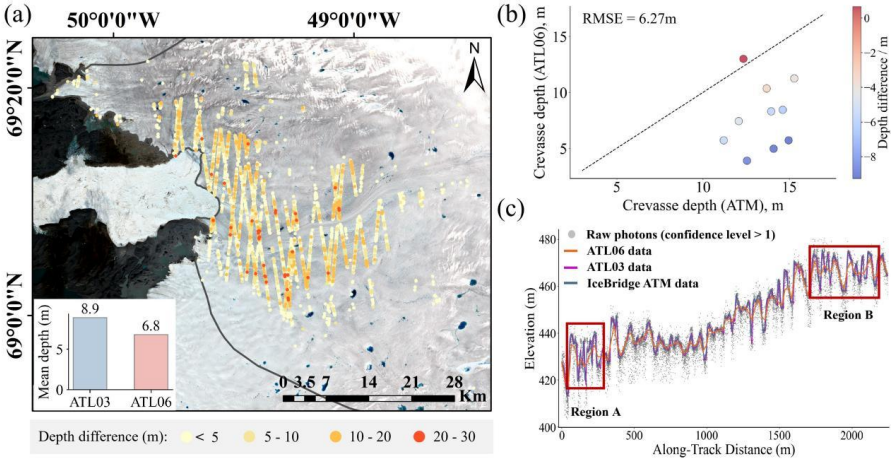

Figure 12. Comparison between crevasse depth estimation results based on ATL03 and ATL06 products. (a) Crevasse depth differences extracted simultaneously by ATL03 and ATL06 products. (b) RMSE for crevasse depth results derived from the ATL06 product and Icebridge ATM point clouds (acquired on the same day). (c) Photon track of ICESat-2 ATL03, ATL06 and Icebridge ATM point clouds.

5.2 Comparison with crevasse depths derived from ArcticDEM

Elevation products generated by satellite stereophotogrammetry, such as ArcticDEM, can be used to extract crevasse depths and have already been successfully applied across the GrIS (Chudley et al., 2021, 2025). However, they are still limited by several factors, such as the low texture contrast of the glacier surface and the lack of light at the bottom and sidewalls of crevasses, which often leads to failures or underestimations in detecting crevasse depth. To compare the differences between ICESat-2 and ArcticDEM in crevasse depth detection, we manually interpreted 16 crevasses in the elevation profiles, as shown in Fig. 13a. Although there is a 10-day time difference between the selected ArcticDEM strip data (April 10, 2019) and the ATL03 data (April 20, 2019), the overall trend of the elevation profiles from both datasets is consistent, and the corresponding profiles were manually matched. Figure 13b shows the depths of 16 manually extracted crevasses and their differences. The

https://doi.org/10.5194/egusphere-2026-2598
Preprint. Discussion started: 20 May 2026

results indicate that the crevasse depths derived from ATL03 are generally deeper than those from the ArcticDEM, with an average depth difference of 1.40 m. This suggests that our method can not only complement existing datasets by capturing meter-scale crevasses, but also potentially provide new insights into the role of crevasse depth in ice dynamics and calving studies.

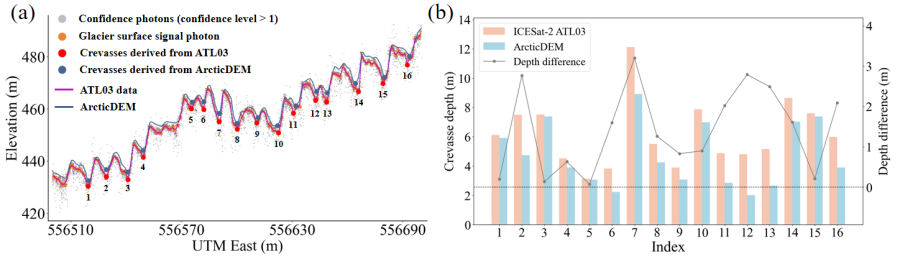

Figure 13. Comparison of crevasse depth estimation results based on ATL03 and ArcticDEM. (a) Elevation profiles and crevasse detection results from ATL03 and ArcticDEM (ArcticDEM strip data: SETSM_s2s041_WV03_20190410_1040010049CC9200_1040010004C8E3900_2m_lsf_seg1_dem.tif, and ATL03 data: ATL03_20190420093051_03380303_006_02.h5/gt2l). (b) The depth of crevasses detected by ATL03 and ArcticDEM and their differences.

5.3 Implications and limitations

In this study, we propose an automated and efficient method for crevasse extraction and depth estimation from the ICESat-2 ATL03 product. Unlike previous studies that focused on large crevasses in Antarctic ice shelves using the ATL06 product (Li et al., 2021; Wang et al., 2021), the proposed method can more accurately detect crevasses of varying sizes and estimate their depths. To the best of our knowledge, this is the first study to map crevasse depths from ICESat-2 over the GrIS. Comprehensive experiments demonstrate that the proposed method achieves an excellent performance for detecting crevasse locations and their depths from the ICESat-2 ATL03 product contaminated by noises. In addition, mapping the crevasse depth distribution in SKJI further demonstrates the applicability of the proposed method to large-scale regions and

https://doi.org/10.5194/egusphere-2026-2598
Preprint. Discussion started: 20 May 2026

reveals the spatial characteristics of crevasse depth distribution and their potential implications for glacier stability. Overall, this work provides an effective approach for large-scale crevasse depth mapping and can be extended to other glacierized regions worldwide, such as the polar regions and mountain glaciers.

There are nevertheless several limitations in this study. Although ICESat-2 has an ultra-high resolution of 0.7 m, providing an unprecedented opportunity to detect small crevasses, it can only measure their visible depths rather than the full structural depths. In future work, the observed visible depths derived from ICESat-2 can be used to constrain and validate physical or numerical models to better estimate actual crevasse depths. This will be significant for revealing the evolution of crevasses.

6. Conclusions

This study demonstrates the capability of ICESat-2 ATL03 data for mapping crevasse depths at a basin scale. Such information can provide critical insights into glacier dynamics, meltwater transport, and calving behavior. We developed an automated and rapid method for quantifying crevasse depths, which includes rapid detection of crevassed regions, glacier-height retrieval, and crevasse extraction and depth estimation. This is a new and effective way to identify crevasses and extract their metrics, and is the first use of ICESat-2 ATL03 data to map crevasse depths at the basin scale on the GrIS. We successfully applied the method to 104 ICESat-2 ATL03 data tracks across SKJI in 2019. Quantitative comparison with IceBridge airborne altimetry data and visual comparison with Planet imagery demonstrates that our method works well for detecting crevasse locations and their depths from the ICESat-2 ATL03. A total of 18,775 crevasse locations were identified, and the crevasses were mainly distributed below 900 m a.s.l. in the south ice stream and below 600 m a.s.l. in the north. The depth maxima occur at approximately 20 km and 10 km inland in the south and north ice streams, respectively. In addition, crevasse depths derived from our method are approximately 28% and 30% deeper than those obtained from ATL06 and ArcticDEM, respectively.

https://doi.org/10.5194/egusphere-2026-2598
Preprint. Discussion started: 20 May 2026

Our algorithm has the potential to map crevasse locations and depths in other regions, including Antarctica and mountain glaciers. In addition, the visible crevasse depths obtained from ICESat-2 provide useful observational constraints for future physical and numerical modelling of crevasse evolution, which may help to better quantify the role of crevasses in ice dynamics and predict their contribution to future mass loss and sea level rise.

Data availability

The Ice, Cloud, and land Elevation Satellite-2 (ICESat-2) ATL03 and ATL06 data used in this study are publicly available from the National Snow and Ice Data Center (NSIDC): https://nsidc.org/data/atl03/versions/6 and https://nsidc.org/data/atl06/versions/6 (Neumann et al., 2023; Smith et al., 2023). ArcticDEM data are available from the Polar Geospatial Center: https://www.pgc.umn.edu/data/arcticdem/ (Porter et al., 2023). Ice velocity maps are from Solgaard et al. (2021). NASA IceBridge ATM data are publicly available from the NSIDC Operation IceBridge Data Portal (https://nsidc.org/data/ilatm1b/versions/2, last access: 5 May 2026).

.

Author contributions

Conceptualization: RH, LJ. Methodology:RC, RH. Formal analysis: RC, XL, RH, AJS, SJL, and LJ. Data interpretation: all authors. Writing-original draft:RC. Writing-review and editing: all authors.

Competing interests

At least one of the (co-)authors is a member of the editorial board of The Cryosphere.

Disclaimer

https://doi.org/10.5194/egusphere-2026-2598
Preprint. Discussion started: 20 May 2026

Publisher's note: Copernicus Publications remains neutral with regard to jurisdictional claims in published maps and institutional affiliations.

Acknowledgments

We acknowledge support from the ICESat-2 Projects for making data available for this research, and the reviewers for making time to review and comment on the manuscript.

Financial support

This work was supported by the National Natural Science Foundation of China (No. 42171443) ; the Youth Innovation Promotion Association of the Chinese Academy of Sciences (No. 2023348); Science Fund for Distinguished Young Scholars of Hubei Province (No. 2023AFA104).

References

Abshire, J. B., Sun, X., Riris, H., Sirota, J. M., McGarry, J. F., Palm, S., Yi, D., and Liiva, P.: Geoscience Laser Altimeter System (GLAS) on the ICESat mission: on-orbit measurement performance, Geophys. Res. Lett., 32, L21S02, https://doi.org/10.1029/2005GL024028, 2005.

Barrand, N. E., Murray, T., James, T. D., Barr, S. L., and Mills, J. P.: Optimizing photogrammetric DEMs for glacier volume change assessment using laser-scanning derived ground-control points, J. Glaciol., 55, 106–116, https://doi.org/10.3189/002214309788609001, 2009.

Bassis, J. N. and Ma, Y.: Evolution of basal crevasses links ice shelf stability to ocean forcing, Earth Planet. Sci. Lett., 409, 203–211, https://doi.org/10.1016/j.epsl.2014.11.003, 2015.

Benn, D. I., Warren, C. R., and Mottram, R. H.: Calving processes and the dynamics of calving glaciers, Earth Sci. Rev., 82, 143–179, https://doi.org/10.1016/j.earscirev.2007.02.002, 2007.

Berg, B. and Bassis, J.: Crevasse advection increases glacier calving, J. Glaciol., 68, 977–986, https://doi.org/10.1017/jog.2022.10, 2022.

Chandler, D. M. and Hubbard, A.: Widespread partial-depth hydrofractures in ice sheets driven by supraglacial streams, Nat. Geosci., 16, 605–611, https://doi.org/10.1038/s41561-023-01208-0, 2023.

https://doi.org/10.5194/egusphere-2026-2598
Preprint. Discussion started: 20 May 2026

Chang, R., Huang, R., Jiang, L., Dong, Z., and Wang, H.: A robust density estimation method for glacier-height retrieval from ICESat-2 photon-counting data, IEEE Trans. Geosci. Remote Sens., 61, 1–17, https://doi.org/10.1109/TGRS.2023.3277008, 2023.

Chudley, T. R., Christoffersen, P., Doyle, S. H., Dowling, T., Law, R., Schoonman, C., Bougamont, M., and Hubbard, B.: Controls on water storage and drainage in crevasses on the Greenland ice sheet, J. Geophys. Res. Earth Surf., 126, e2021JF006287, https://doi.org/10.1029/2021JF006287, 2021.

Chudley, T. R., Howat, I. M., King, M. D., and MacKie, E. J.: Increased crevassing across accelerating Greenland Ice Sheet margins, Nat. Geosci., 18, 148–153, https://doi.org/10.1038/s41561-024-01636-6, 2025.

Colgan, W., Steffen, K., McLamb, W. S., Abdalati, W., Rajaram, H., Motyka, R., Phillips, T., and Anderson, R.: An increase in crevasse extent, West Greenland: hydrologic implications, Geophys. Res. Lett., 38, L18502, https://doi.org/10.1029/2011GL048491, 2011.

Fountain, A. G., Jacobel, R. W., Schlichting, R. B., and Jansson, P.: Fractures as the main pathways of water flow in temperate glaciers, Nature, 433, 618–621, https://doi.org/10.1038/nature03296, 2005.

Fricker, H. A., Bassis, J. N., Minster, B., and MacAyeal, D. R.: ICESat's new perspective on ice shelf rifts: the vertical dimension, Geophys. Res. Lett., 32, L23S08, https://doi.org/10.1029/2005GL025070, 2005.

Herzfeld, U. C., Trantow, T., Lawson, M., Hans, J., and Medley, G.: Surface heights and crevasse morphologies of surging and fast-moving glaciers from ICESat-2 laser altimeter data: application of the density-dimension algorithm (DDA-ice) and evaluation using airborne altimeter and Planet SkySat data, Sci. Remote Sens., 3, 100013, https://doi.org/10.1016/j.srs.2020.100013, 2021.

Hingee, K. L., Caccetta, P., and Caccetta, L.: Modelling discontinuous terrain from DSMs using segment labelling, outlier removal and thin-plate splines, ISPRS J. Photogramm. Remote Sens., 155, 159–171, https://doi.org/10.1016/j.isprsjprs.2019.07.004, 2019.

Huang, R., Jiang, L., Wang, H., and Yang, B.: A bidirectional analysis method for extracting glacier crevasses from airborne LiDAR point clouds, Remote Sens., 11, 2373, https://doi.org/10.3390/rs11202373, 2019.

Jones, G. A., Ferreira, A. M. G., Kulessa, B., and others: Uppermost crustal structure regulates the flow of the Greenland Ice Sheet, Nat. Commun., 12, 7307, https://doi.org/10.1038/s41467-021-27537-5, 2021.

Joughin, I., Smith, B. E., Howat, I. M., Floricioiu, D., Alley, R. B., Truffer, M., and Fahnestock, M.: Seasonal to decadal scale variations in the surface velocity of Jakobshavn Isbræ, Greenland: observation and model-based analysis, J. Geophys. Res. Earth Surf., 117, F02030, https://doi.org/10.1029/2011JF002110, 2012.

Joughin, I., Smith, B. E., Shean, D. E., and Floricioiu, D.: Brief communication: further summer speedup of Jakobshavn Isbræ, Cryosphere, 8, 209–214, https://doi.org/10.5194/tc-8-209-2014, 2014.

https://doi.org/10.5194/egusphere-2026-2598
Preprint. Discussion started: 20 May 2026

King, M. D., Howat, I. M., Candela, S. G., and others: Dynamic ice loss from the Greenland Ice Sheet driven by sustained glacier retreat, Commun. Earth Environ., 1, 1, https://doi.org/10.1038/s43247-020-0001-2, 2020.

Lai, C. Y., Kingslake, J., Wearing, M. G., and others: Vulnerability of Antarctica's ice shelves to meltwater-driven fracture, Nature, 584, 574–578, https://doi.org/10.1038/s41586-020-2627-8, 2020.

Lampkin, D. J., Amador, N., Parizek, B. R., Farness, K., and Jezek, K.: Drainage from water-filled crevasses along the margins of Jakobshavn Isbræ: a potential catalyst for catchment expansion, J. Geophys. Res. Earth Surf., 118, 795–813, https://doi.org/10.1002/jgrf.20039, 2013.

Li, G., Guo, J., Pei, L., Zhang, S., Tang, X., and Yao, J.: Extraction and analysis of the three-dimensional features of crevasses in the Amery Ice Shelf based on ICESat-2 ATL06 data, IEEE J. Sel. Top. Appl. Earth Obs. Remote Sens., 14, 5796–5806, https://doi.org/10.1109/JSTARS.2021.3085302, 2021.

Liu, Y., Cheng, X., Hui, F., and others: Detection of crevasses over polar ice shelves using satellite laser altimeter, Sci. China Earth Sci., 57, 1267–1277, https://doi.org/10.1007/s11430-013-4796-x, 2014.

Markus, T., Neumann, T., Martino, A., Abdalati, W., Brunt, K., Csatho, B., Farrell, S., Fricker, H. A., Gardner, A., Harding, D., Jasinski, M., Kwok, R., Magruder, L., Lubin, D., Luthcke, S., Morison, J., Nelson, R., Neuenschwander, A., Palm, S., Popescu, S., Shum, C. K., Schutz, B. E., Smith, B. E., Yang, Y., and Zwally, J.: The Ice, Cloud, and land Elevation Satellite-2 (ICESat-2): science requirements, concept, and implementation, Remote Sens. Environ., 190, 260–273, https://doi.org/10.1016/j.rse.2016.12.029, 2017.

Mayer, H. and Herzfeld, U. C.: Structural glaciology of the fast-moving Jakobshavn Isbræ, Greenland, compared to the surging Bering Glacier, Alaska, U.S.A., Ann. Glaciol., 30, 243–249, https://doi.org/10.3189/172756400781820543, 2000.

Mouginot, J., Rignot, E., Bjørk, A. A., van den Broeke, M., Millan, R., Morlighem, M., Noël, B., Scheuchl, B., and Wood, M.: Forty-six years of Greenland Ice Sheet mass balance from 1972 to 2018, Proc. Natl. Acad. Sci. U.S.A., 116, 9239–9244, https://doi.org/10.1073/pnas.1904242116, 2019.

Neumann, T. A., Martino, A. J., Markus, T., Bae, S., Bock, M. R., Brenner, A. C., Brunt, K. M., Cavanaugh, J., Fernandes, S. T., Hancock, D. W., Harbeck, K., Lee, J., Kurtz, N. T., Luers, P. J., Luthcke, S. B., Magruder, L., Pennington, T. A., Ramos-Izquierdo, L., Rebold, T., Skoog, J., and Thomas, T. C.: The Ice, Cloud and Land Elevation Satellite–2 mission: a global geolocated photon product derived from the Advanced Topographic Laser Altimeter System, Remote Sens. Environ., 233, 111325, https://doi.org/10.1016/j.rse.2019.111325, 2019.

Picton, H. J., Nienow, P. W., Slater, D. A., and Chudley, T. R.: A reassessment of the role of atmospheric and oceanic forcing on ice dynamics at Jakobshavn Isbræ (Sermeq Kujalleq), Ilulissat Icefjord, J. Geophys. Res. Earth Surf., 130, e2024JF008104, https://doi.org/10.1029/2024JF008104, 2025.

https://doi.org/10.5194/egusphere-2026-2598
Preprint. Discussion started: 20 May 2026

Podlech, S. and Weidick, A.: A catastrophic break-up of the front of Jakobshavn Isbræ, West Greenland, 2002/03, J. Glaciol., 50, 153–154, https://doi.org/10.3189/172756504781830231, 2004.

Porter, C., Howat, I., Noh, M.-J., Husby, E., Khuvis, S., Danish, E., Tomko, K., Gardiner, J., Negrete, A., Yadav, B., Klassen, J., Kelleher, C., Cloutier, M., Bakker, J., Enos, J., Arnold, G., Bauer, G., Morin, P. 2023. ArcticDEM - Mosaics, Version 4.1. In P.G. Center (Ed.): Harvard Dataverse

Rignot, E. and Kanagaratnam, P.: Changes in the velocity structure of the Greenland Ice Sheet, Science, 311, 986–990, https://doi.org/10.1126/science.1121381, 2006.

Ryan, J. C., Hubbard, A. L., Box, J. E., Todd, J., Christoffersen, P., Carr, J. R., Holt, T. O., and Snooke, N.: UAV photogrammetry and structure from motion to assess calving dynamics at Store Glacier, a large outlet draining the Greenland ice sheet, Cryosphere, 9, 1–11, https://doi.org/10.5194/tc-9-1-2015, 2015.

Semple, A.G., Tan, B., Lin, G. 2023. Geometric Assessment of PlanetScope Imagery. In, *23rd Annual American Geophysical Union (AGU) Meeting*

Shepherd, A. I. T.: Mass balance of the Greenland Ice Sheet from 1992 to 2018, Nature, 579, 233–239, https://doi.org/10.1038/s41586-019-1855-2, 2020.

Smith, B., and others: Pervasive ice sheet mass loss reflects competing ocean and atmosphere processes, Science, 368, 1239–1242, https://doi.org/10.1126/science.aaz5845, 2020.

Smith, B., Fricker, H. A., Holschuh, N., Gardner, A. S., Adusumilli, S., Brunt, K. M., Csatho, B., Harbeck, K., Huth, A., Neumann, T., Nilsson, J., and Siegfried, M. R.: Land ice height-retrieval algorithm for NASA's ICESat-2 photon-counting laser altimeter, Remote Sens. Environ., 233, 111352, https://doi.org/10.1016/j.rse.2019.111352, 2019.

Sohn, H. G., Jezek, K. C., and van der Veen, C. J.: Jakobshavn Glacier, West Greenland: 30 years of spaceborne observations, Geophys. Res. Lett., 25, 2699–2702, https://doi.org/10.1029/98GL01973, 1998.

Solgaard, A.M., Kusk, A. 2022. Greenland Ice Velocity from Sentinel-1 Edition 3. In: GEUS Dataverse

Vaughan, D. G.: Relating the occurrence of crevasses to surface strain rates, J. Glaciol., 39, 255–266, https://doi.org/10.3189/S0022143000015926, 1993.

Walker, C. C. and Gardner, A. S.: Evolution of ice shelf rifts: implications for formation mechanics and morphological controls, Earth Planet. Sci. Lett., 526, 115764, https://doi.org/10.1016/j.epsl.2019.115764, 2019.

Wang, S., Alexander, P., Wu, Q., Tedesco, M., and Shu, S.: Characterization of ice shelf fracture features using ICESat-2 – a case study over the Amery Ice Shelf, Remote Sens. Environ., 255, 112266, https://doi.org/10.1016/j.rse.2020.112266, 2021.

Williams, R. M., Ray, L. E., Lever, J. H., and Burzynski, A. M.: Crevasse detection in ice sheets using ground penetrating radar and machine learning, IEEE J. Sel. Top. Appl. Earth Obs. Remote Sens., 7, 4836–4848, https://doi.org/10.1109/JSTARS.2014.2332872, 2014.

https://doi.org/10.5194/egusphere-2026-2598
Preprint. Discussion started: 20 May 2026

749 Zarrinderakht, M., Schoof, C., and Peirce, A.: The effect of hydrology and crevasse
750 wall contact on calving, Cryosphere, 16, 4491–4512, https://doi.org/10.5194/tc-16-
751 4491-2022, 2022.
752 Zhang, W., Yang, K., Smith, L. C., Wang, Y., van As, D., Noël, B., Lu, Y., and Liu, J.:
753 Pan-Greenland mapping of supraglacial rivers, lakes, and water-filled crevasses in a
754 cool summer (2018) and a warm summer (2019), Remote Sens. Environ., 297,
755 113781, https://doi.org/10.1016/j.rse.2023.113781, 2023.
756 Zhao, J., Liang, S., Li, X., Duan, Y., and Liang, L.: Detection of surface crevasses over
757 Antarctic ice shelves using SAR imagery and deep learning method, Remote Sens.,
758 14, 487, https://doi.org/10.3390/rs14030487, 2022.
759